CrystEngComm

Single Crystal Ferroelectric AlScN Nanowires

Journal:	*CrystEngComm*
Manuscript ID	CE-ART-10-2023-000990.R1
Article Type:	Paper
Date Submitted by the Author:	21-Nov-2023
Complete List of Authors:	Zhang, Xiaoman; Louisiana State University, Mechanical and Industrial Engineering Department Xu, Wangwang; Louisiana State University System Meng, Wen; Louisiana State University, Mechanical and Industrial Engineering Department Meng, Andrew; University of Missouri, Physics and Astronomy

ARTICLE

Single Crystal Ferroelectric AlScN Nanowires

Xiaoman Zhang[a], Wangwang Xu[a], W. J. Meng[a*], Andrew C. Meng[b*]

Received 00th January 20xx,
Accepted 00th January 20xx

DOI: 10.1039/x0xx00000x

Despite the considerable potential and significant promise of aluminum scandium nitride (AlScN) ferroelectric materials for neuromorphic computing applications, challenges related to device engineering, along with the considerable structural disorder in thin films grown on various substrates using different vapor synthesis methods, make it difficult to systematically study the structure-property relationship. In this work, we approach such issues from the crystal growth side by successfully growing high-quality single crystal AlScN nanowires through ultra-high vacuum reactive sputtering under high substrate bias and low atomic flux conditions, which leads to simultaneous growth and etching. Characterization of nanowire arrays using X-ray diffraction and transmission electron microscopy shows that the wires are epitaxial single crystals with significantly reduced mosaic spread and predominantly single ferroelectric domains. Moreover, ferroelectric and piezoelectric properties were evaluated using Piezoresponse Force Microscopy. The single crystal AlScN nanowires show an out-of-plane piezoelectric constant d_{33} that is greater than 20 pm/V, which is higher than that of pure AlN by a factor of ~4.

Introduction

AlScN ferroelectrics show significant promise for use in wide-ranging device applications, including random-access memory[1-3] and acoustic resonators.[4-6] Epitaxial growth of AlScN thin films on a wide range of substrates and buffer layers, including Si(111),[7] Al_2O_3(0001),[8, 9] Al_2O_3(0001)/Mo(110),[10] SiC,[4, 11] and GaN(0001)[12-14] have been reported. More commonly, columnar polycrystalline AlScN thin films are grown on a variety of textured metallic bottom electrodes deposited onto Si wafers.[2, 15, 16] Interestingly, the mosaic spread of epitaxial single crystals[7] and columnar nanocrystals[17, 18] are about the same, on the order of several degrees. This fact has been well documented and attributed to several factors: 1) lattice mismatch between AlScN and the substrate (or the buffer layer on which it is grown) results in a high density of crystallographic defects, such as dislocations;[19] 2) island nucleation/Volmer-Weber growth[20, 21] leads to mosaic domains that, while on-average exhibiting in- and out-of-plane orientational registry with the bulk substrate, are misoriented from each other; 3) complexity of the film/substrate heterointerface.[7, 10, 22] The last factor, particularly in polycrystalline materials, can be difficult to characterize structurally due to the simultaneous variation in multiple structural parameters. Consequently, adopting a materials structure-based approach for device optimization, such as reducing electrical leakage in ferroelectric AlScN, proves challenging. The difficulty lies in isolating the effects of individual structural features on the electrical properties.

Several crystal growth methods can be employed to reduce structural disorder. For thin films, one approach involves using selective area growth,[23, 24] which truncates crystallographic defects by creating high-aspect-ratio openings in a hard mask. Epitaxial lateral overgrowth[25-27] is then employed to obtain continuous films. For this to work, it is crucial to select an appropriate material for the mask,[28, 29] ensuring that deposition occurs primarily through the mask's holes on the substrate and minimally on the mask itself. Selective area growth has been reported in numerous studies, utilizing techniques such as chemical vapor deposition (CVD)[30, 31] and molecular beam epitaxy (MBE).[32, 33] Although sputtered films generally exhibit a higher sticking coefficient on substrates, exploiting the difference in nucleation between the substrate and the mask can still enable the achievement of selective area growth.[34-36]

Similar to selective area growth, nanowire growth offers another pathway to decreased structural variation and defects.[37-40] The small areal cross-section of wire growth minimizes effects of lattice mismatch, and finite size effects help limit the presence of mosaic domain structure when the nanowire radius approaches the average domain size. CVD and MBE growth of epitaxial nanowires has been used to synthesize defect-free single crystal III-V nanowires on Si substrates.[33, 40] Growth of III-nitride nanowires has also been demonstrated.[34, 41-43] However, while vapor-liquid-solid (VLS) growth of epitaxial GaN nanowires on Si(111) can be achieved using CVD, MBE, or sputtering, growth of AlN based nanowires is less straightforward.[44] Despite AlN and GaN having similar melting points (3073K and 2493K, respectively),[45, 46] the mobility of surface species differs significantly between AlN and GaN material systems: Ga liquid droplets are known to self-catalyze GaN nanowire growth,[47, 48] whereas the reported growth mechanism for AlN based nanowires varies widely. Observations during sputter deposition of AlN-based nanowires have shown an absence of liquid species.[49]

---

[a] Department of Mechanical and Industrial Engineering, Louisiana State University, Baton Rouge, LA 70803
[b] Department of Physics and Astronomy, University of Missouri, Columbia, MO 65211
* wmeng1@lsu.edu; acmeng@missouri.edu

Electronic Supplementary Information (ESI) available: [details of any supplementary information available should be included here]. See DOI: 10.1039/x0xx00000x

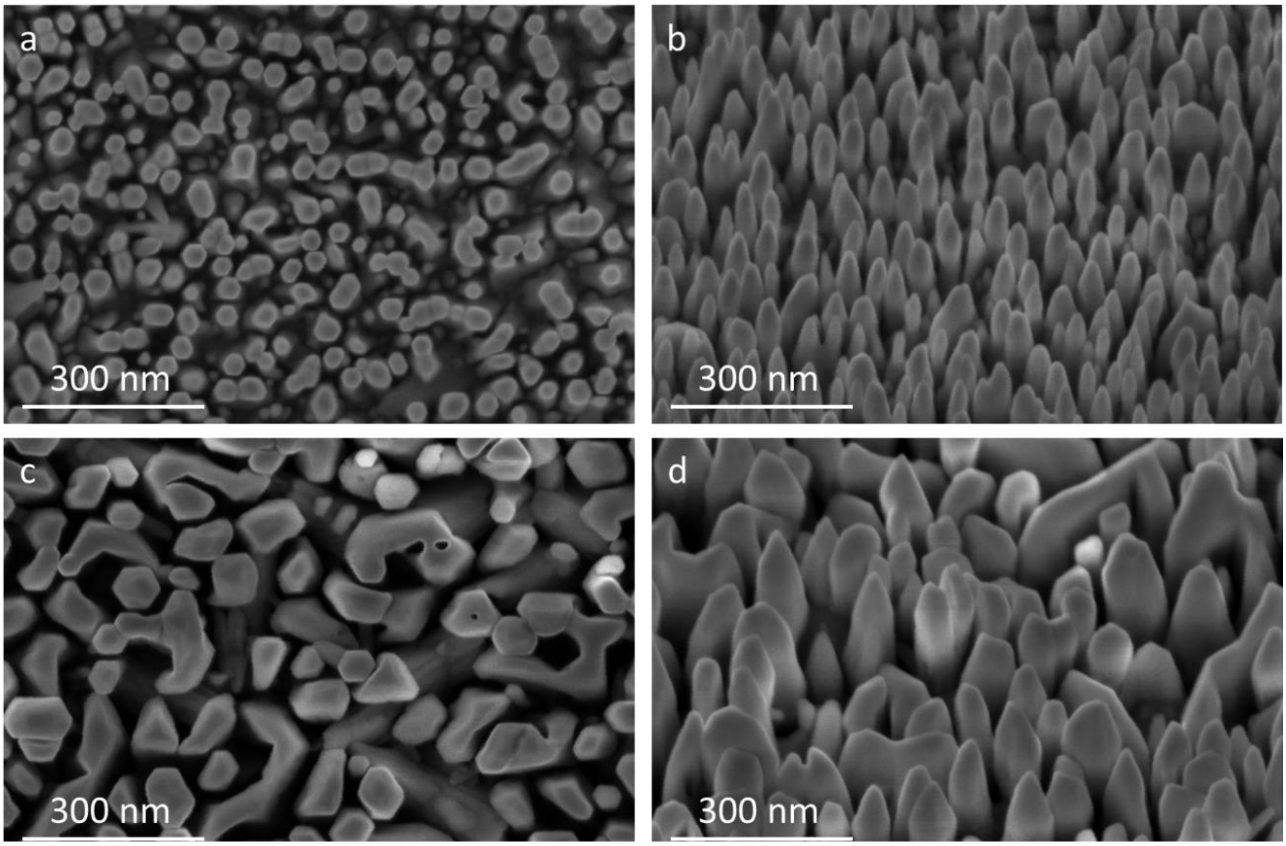

Figure 1. (a) Plan-view and (b) tilted-view SEM images of low Sc concentration AlScN nanowires after a 45 min growth; (c) plan-view and (d) tilted-view SEM images of high Sc concentration AlScN nanowires after a 90 min growth.

Due to the prevalence of sputter-deposited material in most reports of ferroelectric AlScN,[1-3, 50-52] the present work focuses on growing AlScN nanowires using ultra-high vacuum (UHV) reactive sputtering. To achieve this, we employed a combination of substrate bias and gun current to vary ion bombardment and deposition flux, respectively. Such variations led to a growth regime where nanowires, instead of continuous films, are formed through simultaneous growth and etch processes. To confirm the structure of the nanowires, X-ray diffraction (XRD) and Scanning/Transmission Electron Microscopy (S/TEM) were utilized. To further characterize the ferroelectric properties of the AlScN nanowires, differential phase contrast (DPC) STEM imaging and Piezoresponse Force Microscopy (PFM) were employed. These results confirm the ferroelectric nature of the AlScN nanowires.

Results and Discussion

Growth Process

Epitaxial AlScN thin films, when reactively sputtered directly on Si(111), possess significant mosaic spread and structural disorder.[7] Recently, remanent polarization in ferroelectric AlScN has been observed to be inversely correlated with rocking curve full-width at half maximum (FWHM).[53] To mitigate mosaicity in AlScN, we adopted a nanowire growth approach towards achieving a high-quality single crystal ferroelectric material. Substrate bias voltages and gun currents were adjusted to grow AlScN nanowires. In addition, an epitaxial TiN(111) buffer layer[54] on Si(111) was employed, known to promote AlN nanowire growth.[49, 55] Figure 1 shows scanning electron microscopy (SEM) images of AlScN deposited onto the TiN buffer layer under different growth conditions. The plan- and tilted- view SEM images exhibited in Fig. 1 show clearly that the deposited AlScN formed discontinuous nanowires instead of continuous films. Increasing the Sc gun current from 0.05A to 0.1A and extending the growth duration from 45 to 90 minutes, elevating the atomic flux relative to ion bombardment, led to an increase in nanowire diameter (from 33 ± 8 nm to 70 ± 20 nm) and length (from 173 ± 7 nm to 358 ± 44 nm) (Fig. 1 a-d, *vide infra* Fig. 3a, Fig. 4a). Comparing Figs. 1a and 1c shows that, concurrent with the increase in nanowire diameter, more wires are merged. The increase in nanowire length with growth duration indicates that the nanowires are indeed grown and not solely a result of an ion etching processes. Previous reports of sputter-deposited, In-alloyed AlN nanowires proposed that the growth mechanism does not involve a liquid catalyst and that differences in surface mobility of the alloying component play an important role.[49]

Figure 2 shows results of structural characterization of AlScN nanowires using XRD. Symmetric θ/2θ scans (Figs. 2a, 2d) show that, besides the (111) family of peaks for the TiN buffer layer and the Si substrate, the only additional reflections can be indexed to the (0001) basal plane family of reflections for wurtzite AlScN. Asymmetric ϕ scans (Figs. 2b, 2e) show that the 6 TiN (042) reflections are coincident with the 6 Si (513) reflections, and that the 6 AlScN $(10\bar{1}3)$ reflections are offset by 30° from the TiN and Si reflections. The combined information from the θ/2θ scans and

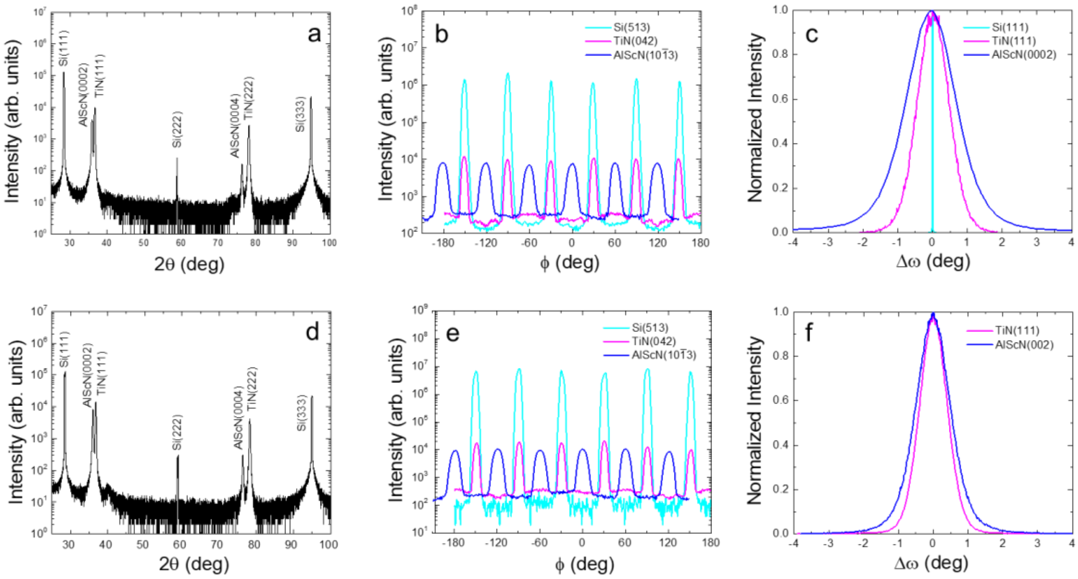

Figure 2. XRD data of AlScN nanowires: (a) θ/2θ, (b) asymmetric ϕ, (c) ω rocking curve scans of the low Sc concentration AlScN nanowires grown for 45 min; (d) θ/2θ, (e) asymmetric ϕ, (f) ω rocking curve scans of the high Sc concentration AlScN nanowires grown for 90 min.

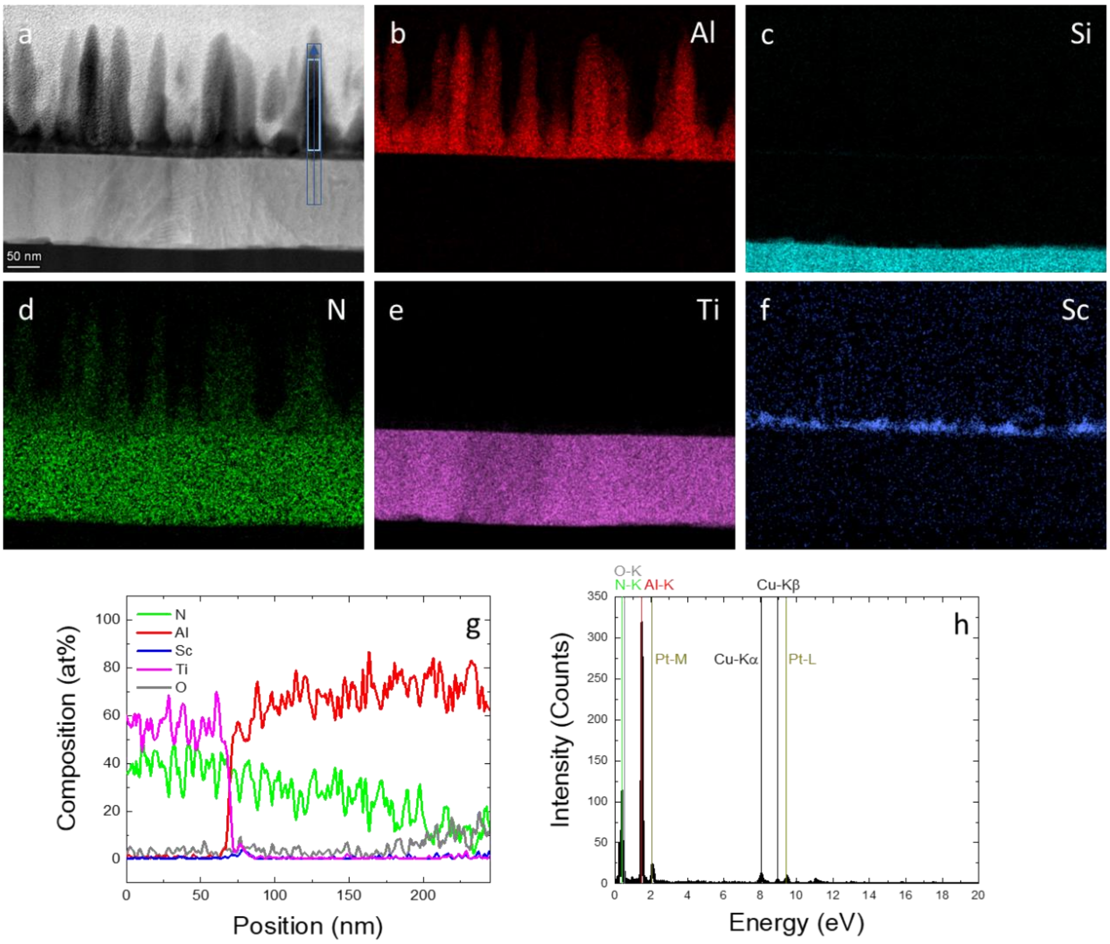

Figure 3. STEM characterization of the low Sc concentration AlScN nanowires after 45 min growth: (a) HAADF-STEM image; STEM-EDS signals of (b) Al, (c) Si, (d) N, (e) Ti, and (f) Sc; (g) STEM-EDS line scan of the dark blue region in (a); (h) EDS spectrum from the dark blue region in (a).

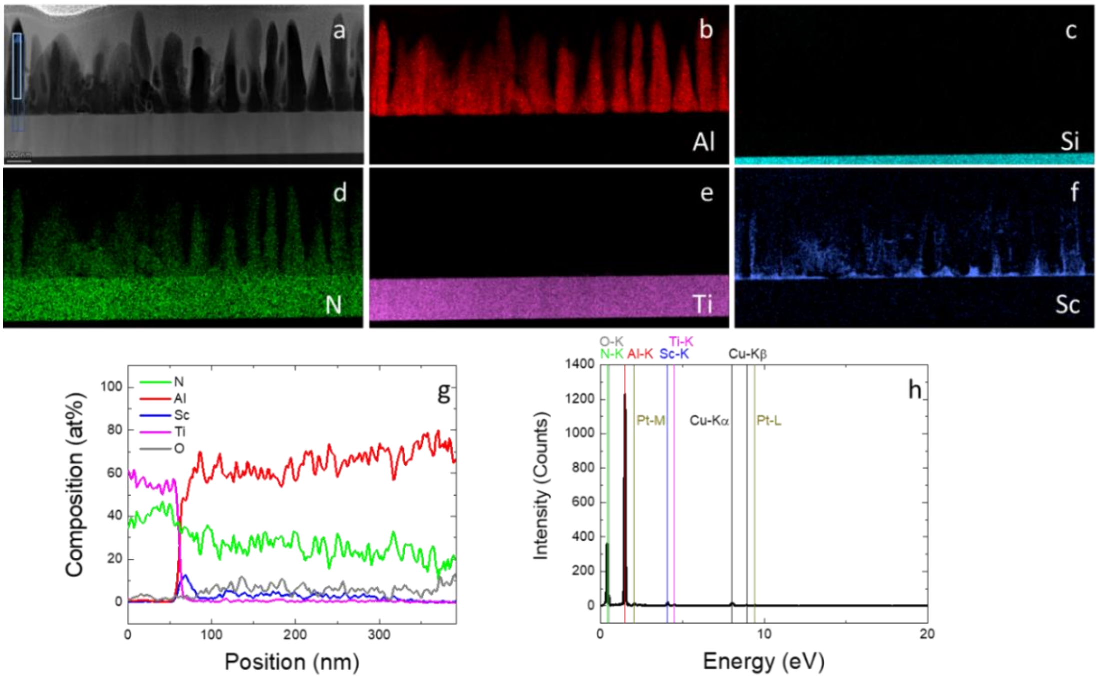

Figure 4. STEM characterization of the high Sc concentration AlScN nanowires after 90 min growth: (a) HAADF-STEM image; STEM-EDS signals of (b) Al, (c) Si, (d) N, (e) Ti, and (f) Sc; (g) STEM-EDS line scan of dark blue region in (a); (h) EDS spectrum from the dark blue region in (a).

asymmetric ϕ scans shows that the AlScN is deposited into the wurtzite structure, and that both the TiN buffer layer and the AlScN wurtzitic nanowires are epitaxial such that AlScN(0001)||TiN(111)||Si(111) and AlScN$(11\bar{2}0)$||TiN$(1\bar{1}0)$||Si$(1\bar{1}0)$. Rocking curves (Figs. 2c, 2f) show that the full-width-at-half-maximum (FWHM) of the AlScN (0002) reflection is only slightly greater (~ 1.68°, 1.14°, respectively) than that of the epitaxial TiN buffer layer (~ 1.06°, 0.90°, respectively). The AlScN rocking curve width is even less than what was reported for epitaxial AlN thin films with no Sc incorporation (1.8°).[7] While the mosaic spread of the TiN buffer layer results from the substantial lattice mismatch between TiN and Si, the present observations suggest that the mosaic spread of the AlScN nanowires results largely from that of the TiN buffer layer, without significant additional contribution from wire growth itself.

The spatial distribution of composition in the AlScN nanowires is characterized using X-Ray Energy Dispersive Spectroscopy (EDS) in STEM. Figures 3b-f show STEM EDS maps of nanowires grown with a lower Sc gun current (0.05A) for 45 min. The Si(111) substrate and epitaxial TiN(111) buffer layer are apparent (Figs. 3 c-e). Notably, the nanowires exhibit a reduced Sc composition compared to their bases, where an AlScN film layer is present (Figs. 3a, f). An EDS linescan shows that the Sc composition near the base is approximately 5 at%, while the Sc composition in the nanowires is at trace level (Fig. 3g). The data is consistent with preferential etching of Sc from AlScN during growth. Figures 4b-f show STEM EDS maps of nanowires grown with a higher Sc gun current (0.1A) for 90 min. While the TiN buffer layer remains consistent, an increase in Sc gun current leads to a significant increase in the Sc composition both at the base of (Al:Sc ~ 5:1) and within the nanowires (Al:Sc ~ 12:1) (Fig. 4g). The nanowire length is also extended due to the longer growth duration. A noteworthy observation is that the Sc composition in the AlScN nanowires is not very uniform, and the Sc composition within the nanowires is significantly lower than in the base. X-ray photoelectron spectroscopy (XPS) data from AlScN nanowires are shown in Supporting Information (Fig. S1). The N 1s (~398 eV) binding energy is consistent with a metal nitride, and the Sc $2p_{3/2}$ (~400eV), and Al 2p (~75 eV) binding energies are higher than than those of the corresponding pure metals and consistent with binding in ScN and AlN, respectively.[56] Electron Energy Loss Spectra (EELS) were also collected on AlScN nanowires: the Al-K absorption edge at ~ 1560eV and the N-K and Sc-L absorption edges at ~400eV were observed (Figs. S2, S3). The combined XPS and EELS data are consistent with nitride formation.[57]

The observed preferential Sc etching is unexpected because the sputter yield of Sc is lower than that of Al.[58] To rationalize the observation of preferential Sc etching, one may look at the enthalpy of formation of AlScN, which can serve as a measure of the cohesive energy that needs to be overcome before sputtering occurs. The positive enthalpy of mixing between wurtzite AlN and rocksalt ScN results in a decrease in magnitude of the enthalpy of formation for wurtzite AlScN, which is negative, as Sc composition increases from 0 at% to a maximum at approximately 25 at% before increasing in magnitude again.[59-62] This indicates that the forces holding atoms of AlScN together decreases as Sc composition increases from 0 at% to ~25 at%, consistent with the observation of preferential etching of higher Sc concentration AlScN compared to lower Sc concentrations. Additionally, it is worth noting that epitaxial thin films with around 20 at% Sc composition have been reported to undergo spinodal decomposition. In AlScN sputter deposited at high temperature, the coupling of this kinetically controlled compositional segregation process with simultaneous growth and etching may lead to spatially non-uniform Sc composition distributions. These factors may be responsible for the unexpected preferential Sc etching behavior observed in the AlScN nanowires.

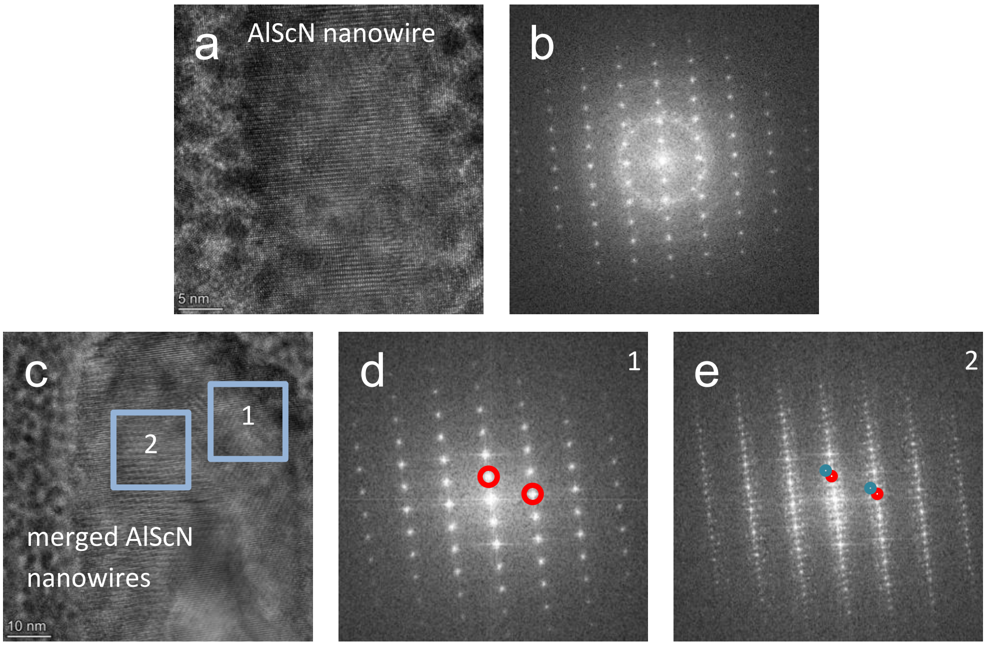

Figure 5. (a) HRTEM of a region containing one low Sc concentration AlScN nanowire and (b) the associated FFT; (c) HRTEM and the corresponding FFTs from (d) region 1 and (e) region 2 of two merged high Sc concentration AlScN nanowires. The red circles in (d) and (e) show the (0001) and $(\bar{1}100)$ reflections; the blue circles in (e) show satellite reflections from Moiré fringes.

High resolution Transmission Electron Microscope (HRTEM) images of the AlScN nanowires and the associated Fast Fourier Transforms (FFTs) are shown in Figure 5. The HRTEM image and the associated FFT of the shorter nanowires with lower Sc composition (Fig. 5a, b) indicate high-quality single crystals exhibiting minimal mosaic spread with the entire nanowire consisting of one single domain. The faint rings in Figure 5b arise from polycrystal the Pt protection layer deposited during the TEM lift-out process. Figure 5c shows an HRTEM image of a region in the longer, higher Sc composition nanowire specimen where two misoriented nanowires merge. Figure 5d shows the FFT of region 1 in Fig. 5c, which is characteristic of one single domain. Figure 5e shows the FFT of region 2 in Fig. 5c, the wire overlap region, which displays satellite reflections typical of Moiré contrast due to two overlapping domains. The region where two wires overlap constitutes a bicrystal boundary between the two wires having the same epitaxial relationship with the substrate but slightly misoriented with respect to one another. Selected Area Electron Diffraction (SAED) from nanowires consistent with the FFT data is shown in the Supporting Information (Fig. S4). Compared to thin films grown using the same technique, the reactively sputtered AlScN nanowires exhibit significantly decreased mosaic spread. Because nanowires largely consist of single domains prior to lateral merging, crystallographic disorder induced by misorientation at mosaic domain boundaries[63] can be dramatically reduced. However, it is currently uncertain what impact lateral overgrowth and nanowire merging induced defects, such as mosaic domain or low angle tilt boundaries, might have on the functional properties of the nanowires.

Figure 6 shows HRTEM images and corresponding FFTs of the AlScN at the base of the nanowires. The AlScN base on top of the TiN buffer exhibits a high level of defects, despite having a reduced lattice mismatch with TiN (approximately +8%) as compared to that with Si (approximately –16%).[19, 54] The FFT from the vicinity of the AlScN/TiN interface (Region 2) in Figure 6a indicates a significant spread in the real-space orientation of the AlScN crystal in this region. A Burger's circuit shown in Figure 6b shows the presence of a dislocation in the AlScN. Similar observations show that the AlScN base region next to the TiN buffer layer is heavily dislocated. In contrast, the AlScN further away from the TiN buffer (Region 3) exhibits fewer crystallographic defects (Fig. 6a, e). Interestingly, the AlScN in the nanowire region (Fig. 5) displays even fewer crystallographic defects. We propose two separate explanations that could account for this observation. One possibility is that, with simultaneous growth and etching, ion bombardment enhances mobility of surface species, especially at the nanowire tips. This would promote reorientation and result in a decreased mosaic spread within a single nanowire. In addition, as ion etching proceeds, the spatial extent of each nanowire becomes smaller than the typical mosaic domain size in a thin film. Another possibility is that the nucleation of misoriented domains can be minimized due to the simultaneous growth and etching process. Over time, a smaller fraction of formed nuclei grows into nanowires, with gaps between them. This could contribute to the observed reduction in crystallographic defects within the nanowires.

Ferroelectric Properties

Recently, differential phase contrast (DPC) in STEM images have been used to map domains in ferroelectric materials.[7, 64-67] By detecting nanoscale spatial variations in the electron beam deflection using a segmented STEM detector, valuable information on the spatial distribution of electric polarization can be obtained. In the case of AlScN nanowires, STEM DPC images show ferroelectric domains for both lower Sc (Figs. 7a-c) and higher Sc (Figs. 7d-f) compositions. In the STEM DPC images, the beam displacement vector direction is indicated by the color, and the magnitude is indicated by the intensity. The presence of contrast in the TiN buffer

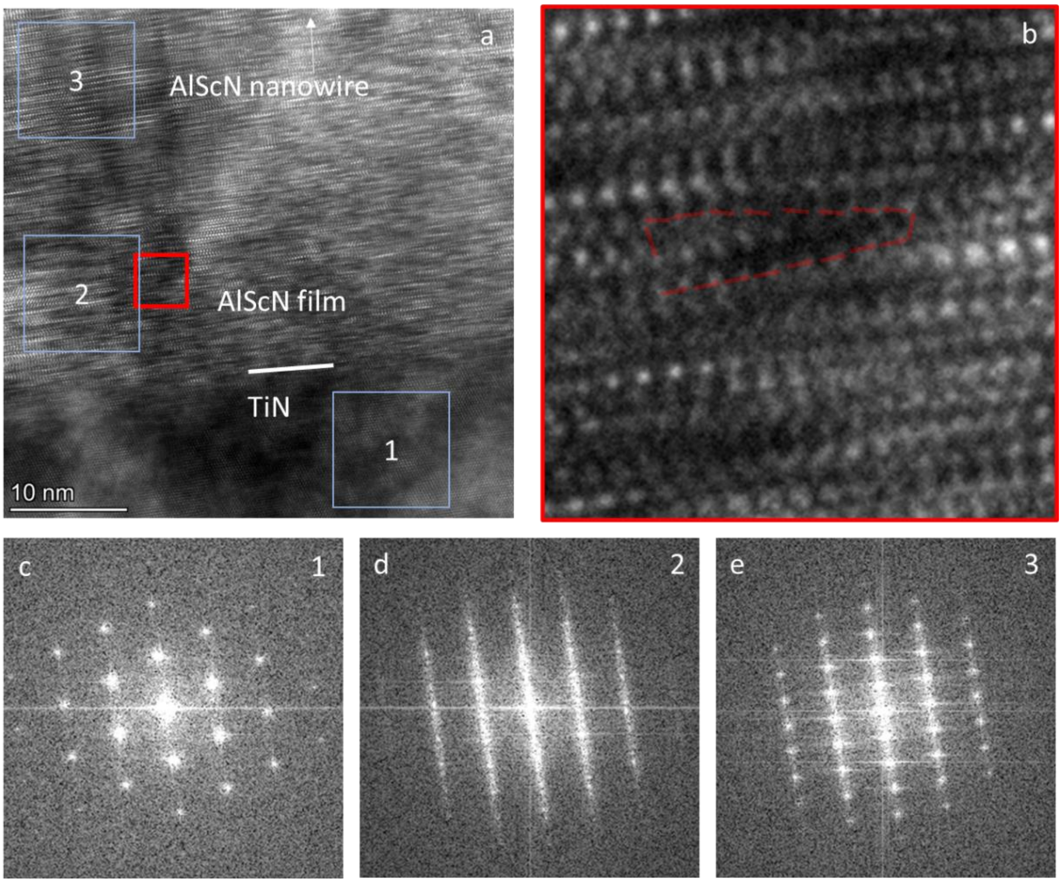

Figure 6. (a) HRTEM of the defective AlScN film region at the base of nanowires, (b) 10× inset of the red region in (a); FFTs from (c) region 1, (d) region 2, and (e) region 3 in (a).

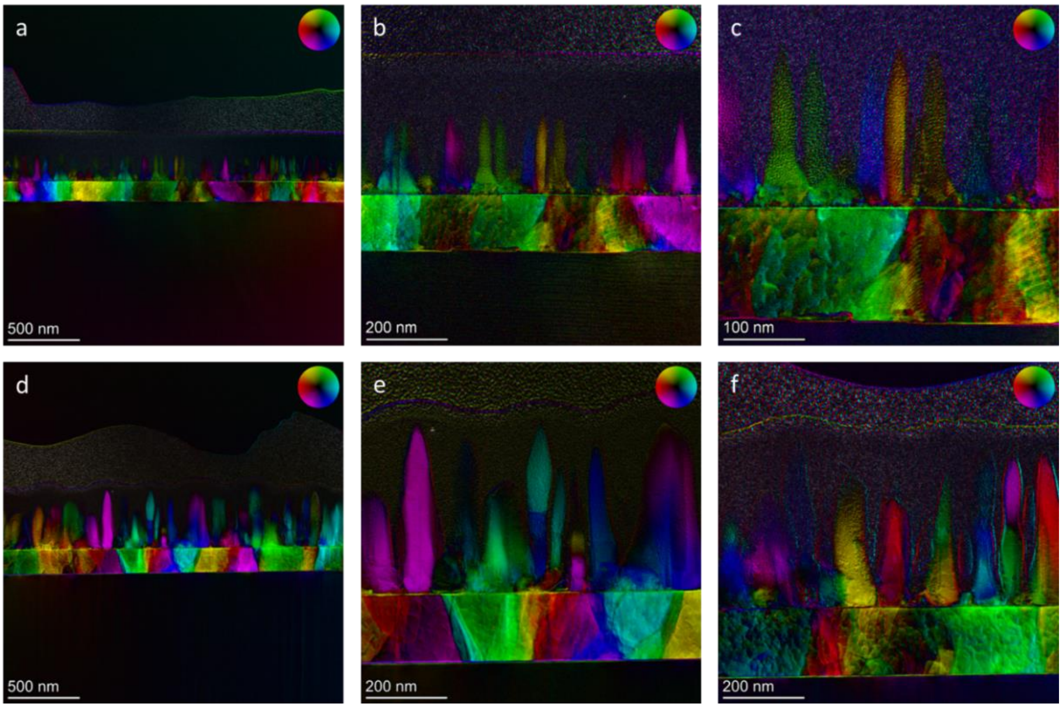

Figure 7. DPC STEM images at different magnifications of the low Sc concentration AlScN nanowires grown for 45 min (a-c) and the higher Sc concentration AlScN nanowires grown for 90 min (d-f).

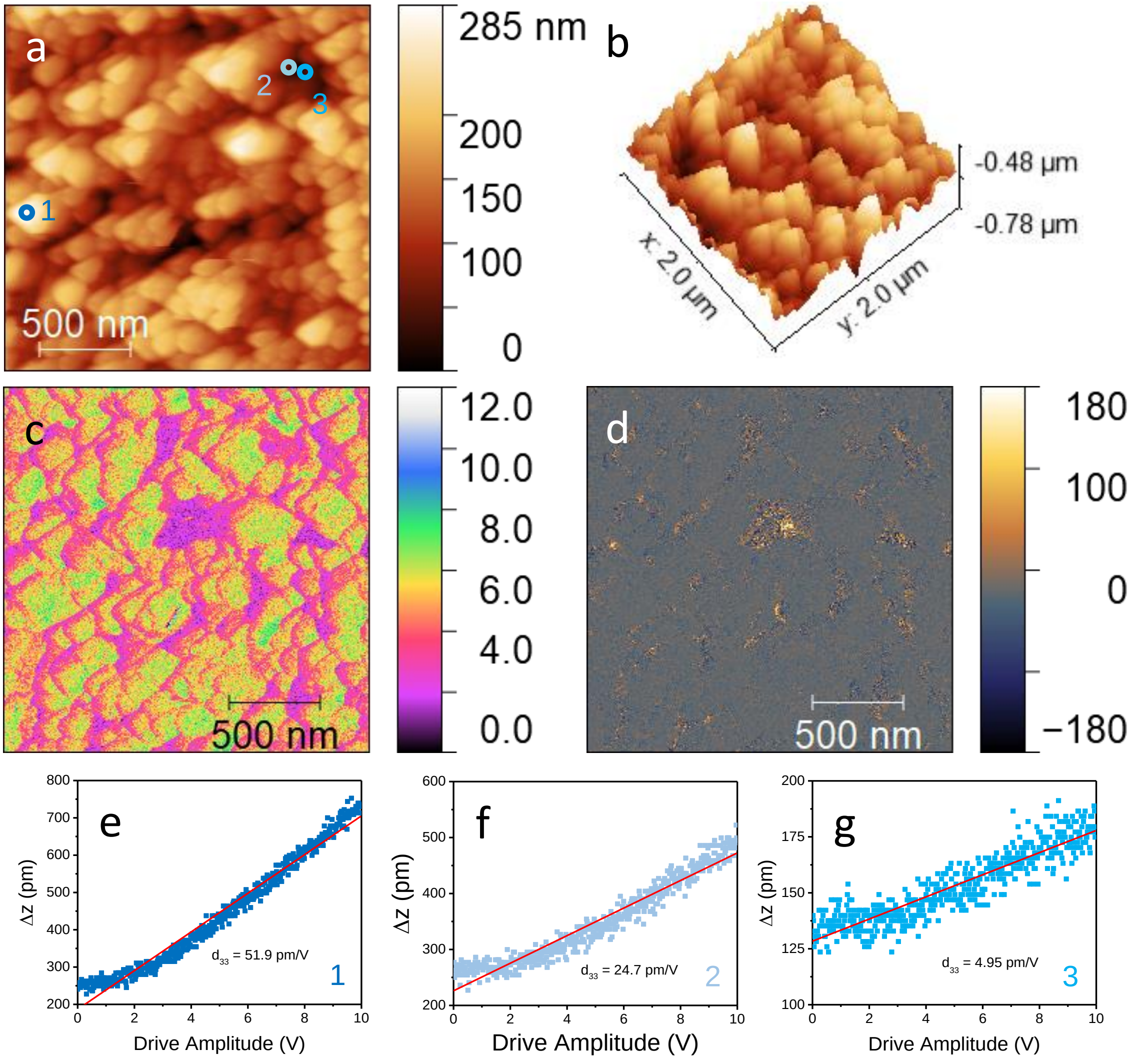

Figure 8. (a-b) AFM topography of the higher Sc concentration AlScN nanowires grown for 90 min; PFM (c) amplitude (mV) and (d) phase (deg) maps of the region in (a-b); ramping measurement of d_{33} in (e) region 1, (f) region 2, and (g) region 3 shown in (a).

layer arises because the TiN(111) surface can be either Ti- or N- polar. For the lower Sc composition nanowires grown for a shorter duration, their DPC images display a uniform single color, indicative of single ferroelectric domains (Figs. 7a-c). However, in the case of the higher Sc composition nanowires, which have undergone longer growth and lateral merging, the DPC images show several nanowires with multiple ferroelectric domains. These domains are observed as multi-colored wire regions in the DPC images (Figs. 7d-f).

To confirm ferroelectricity in the AlScN nanowires, Piezoresponse Force Microscopy (PFM) in conjunction with dc bias poling experiments were performed. Figure 8 displays the piezoelectric response of AlScN nanowires (Sc gun current 0.1A, 90 min growth). The topographical maps (Figs. 8a-b) are consistent with the SEM and STEM images (Figs. 1, 3, and 4). The piezoresponse amplitude and phase are shown in Figs. 8c-d. The contrast aligns well with the topographical image, confirming the piezoelectric response of the nanowires.

Furthermore, the out-of-plane piezoelectric coefficient, d_{33}, was measured on the nanowire samples to vary from 51.9 pm/V on the nanowire (region 1, Fig. 8) to 4.95 pm/V on the AlScN film at the base of the nanowire (region 3, Fig. 8). The d_{33} value was measured to be 24.7 pm/V near the base of a nanowire (region 2, Fig. 8). The lower piezoresponse coefficient of 4.95 pm/V observed on the base AlScN film may be attributable to the presence of a high concentration of crystallographic defects, such as dislocations (Fig. 6). On the other hand, the significantly higher piezoresponse measured at the tip of the nanowire may arise from the dc biased AFM tip inducing mechanical instability, causing the nanowire to bend. This instability could lead to a decrease in the nanowire's height, potentially resulting in an overestimation of d_{33}. The measured value of 24.7 pm/V near the base of the nanowire is closer to what is expected based on the Sc composition.[68-70] This value is also more reasonable, considering the greater mechanical stability of the nanowire base due to its cone shape.

Subsequently, the PFM was employed to apply positive and negative bias to electrically pole regions of the nanowire samples. The resulting contrast, arising from poling, is consistent with ferroelectric behavior. It should be noted here that ionic conductivity can also give rise to similar behavior.[71] Figures 9a and 9b show PFM before and

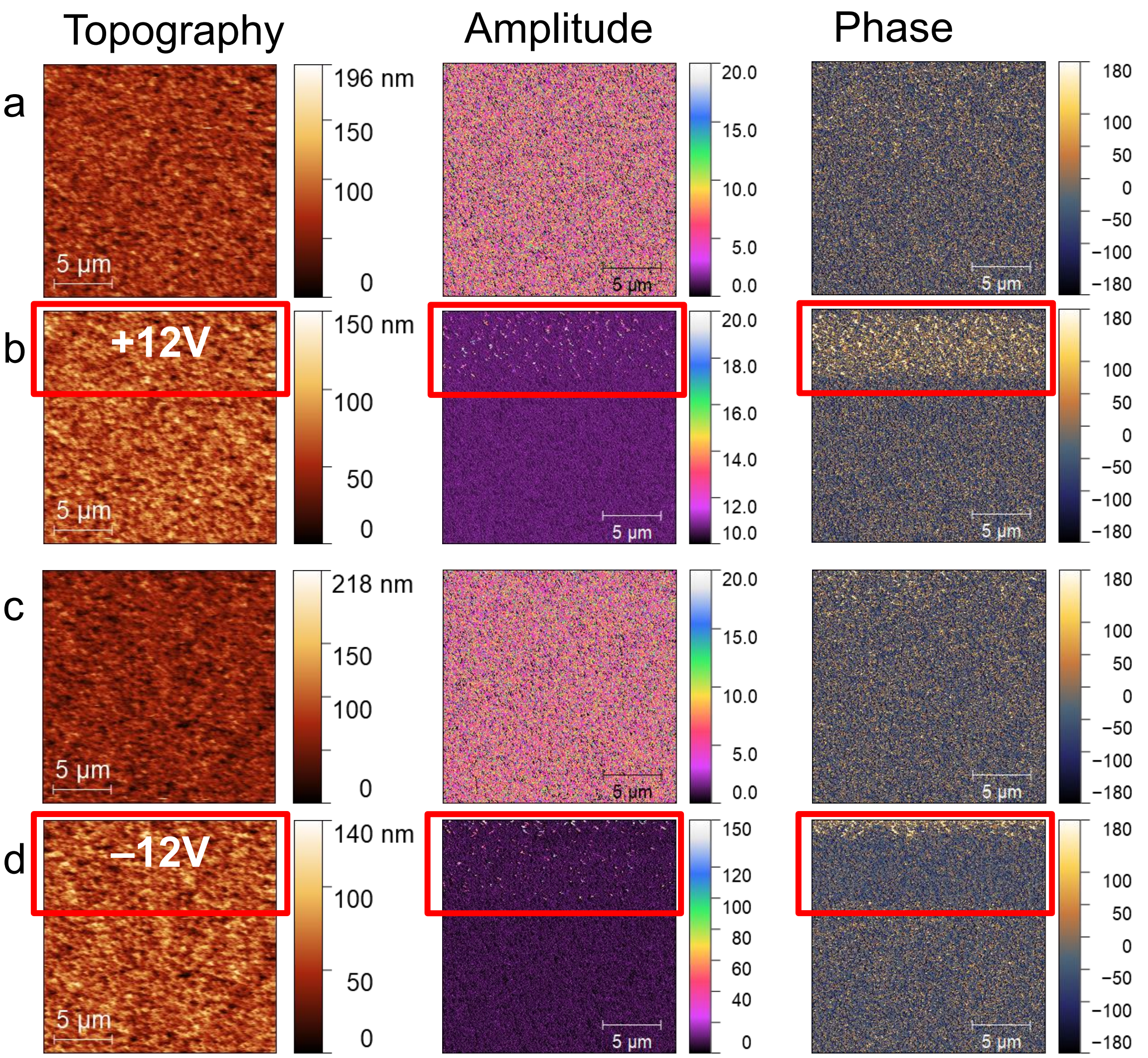

Figure 9. AFM topography, PFM amplitude (mV) and phase (deg) of the same region (a) before and (b) after +12V poling in the area marked by the red rectangle; AFM topography, PFM amplitude and phase of the same region (c) before and (d) after –12V poling in the area marked by the red rectangle.

after poling the sample using +12V. A noticeable contrast change in both amplitude and phase is observed in the poled region (Fig. 9b). Figure 9c and d show PFM before and after poling the sample using –12V. Similarly, a contrast change in both amplitude and phase is observed in the poled region (Fig. 9d), with the phase contrast change being opposite in sign to that when applying a +12V bias (Fig. 9b). The observed contrast changes in amplitude and phase within the poled region are in accordance with ferroelectric behavior of the AlScN nanowires. PFM hysteresis measurements[71, 72] were also performed on AlScN nanowires of both Sc concentrations and a non-ferroelectric control sample. Shown in Supporting Information, these results are also consistent with ferroelectric behavior in the nanowires (Figs. S5, S6, S7).

Nanowire Advantages and Challenges

AlScN ferroelectric materials face significant challenges, in particular regarding electrical leakage and device scaling, which are important concerns for applications.[73] Various engineering-based approaches have been reported to address electrical leakage in sputtered AlScN, such as: using multilayer structures,[74] adjusting the ratio of rf and dc sputtering,[75] and exploring alternative alloying components to replace Sc.[50, 76, 77] Ideally, gaining a fundamental understanding of the structural origins of electrical leakage in AlScN would pave the way for improved functional properties based on the structure-property relationship. However, the presence of mosaic spread-induced crystallographic disorder complicates matters, as rocking curve FWHM has been observed to inversely correlate with remanent polarization in AlScN.[53] This connection between mosaic spread and electrical properties of the material poses a challenge for epitaxial AlScN thin films as well. To address these complexities, the use of single-domain, single-crystal nanowires with minimal mosaic spread offers a promising path for systematically investigating the structure-property relationship in AlScN ferroelectrics. Nanowires bring practical advantages as well. They can serve as seeds for epitaxial lateral overgrowth[23, 26, 78] or enable core-shell heterostructure growth.[38, 39] Additionally, nanowires provide an alternative approach to scaling, potentially offering benefits in reducing electrical leakage due to their reduced mosaic spread and fewer domain boundaries (or grain boundaries). Furthermore, the nanowire's pillar-like shape allows for the utilization of various mechanical testing protocols developed for electromechanical testing in sensors and actuators.

Conclusions

We have demonstrated growth of single crystal epitaxial AlScN nanowires on epitaxial TiN(111) buffered Si(111) using UHV reactive sputtering. The key to this process lies in carefully balancing ion bombardment and atomic flux, which enables simultaneous growth and etching. We show that the small size of the nanowires effectively limits mosaic spread, leading to the formation of predominantly single crystallographic and single ferroelectric domain nanowires. The Sc composition within the nanowires is lower, and we attribute this observation to the decreasing magnitude of the enthalpy of formation of AlScN (a negative quantity) with higher Sc concentrations. The nanowires are ferroelectric, as supported by DPC imaging in the STEM, PFM dc bias poling, and PFM hysteresis experiments. The synthesis of single crystal epitaxial nanowires holds promise for systematically investigating the structure-property relationship in AlScN. Moreover, these nanowires are potentially advantageous for device applications, due to their higher crystal quality and high-aspect-ratio geometry.

Methods

Si(111) wafers were chemically etched in sequential 15.7 M HNO_3 (aq), de-ionized H_2O, 18.4 M HF (aq) solutions with the last step being HF (aq). Wafers were subsequently transferred into an UHV growth chamber with a base pressure of $< 5\times10^{-10}$ Torr through a high-vacuum load lock ($< 1\times10^{-6}$ Torr) and heated in the growth chamber to ~800 °C for ~30 min prior to film deposition. Without changing the substrate temperature, a ~200-nm-thick TiN buffer layer was deposited by sputtering an elemental Ti target (99.995%, Kurt Lesker) in the dc mode at a gun current of 1.3A, in pure N_2 (99.999+%, Airgas) with an input flow rate of 4.5 sccm at a total pressure of ~9.5 mTorr. Immediately following the deposition of the TiN buffer layer, growth of AlScN occurred with an elemental Al target (99.9995%, Kurt Lesker) sputtered in the dc mode at 0.5 A and an elemental Sc target (99.99%, Matsurf Technologies) sputtered in the dc mode at either 0.05 A or 0.1 A. All AlScN growths were also carried out in pure N_2 with an input flow rate of 4.5 sccm at a total pressure of ~9.5 mTorr. A –100 V substrate bias was applied during both TiN and AlScN growth. After growth, the specimens were allowed to cool to room temperature before being transferred out of the growth chamber.

Structural characterization using XRD was performed using a Panalytical Empyrean diffractometer with a χ-ϕ-x-y-z stage using Cu $K\alpha1$ radiation (λ = 1.540598 Å) selected through a 4-bounce Ge(220) monochromator. Symmetric $\theta/2\theta$, asymmetric ϕ, and ω rocking curve scans were collected using a PIXcel-3D detector. SEM characterization was performed using a ThermoFisher Helios G4 dual beam Xe plasma focused ion beam/scanning electron microscope (PFIB/SEM). TEM sample preparation was performed using a ThermoFisher Scios FIB/SEM. The sample was protected from the ion beam during the thinning process through electron beam induced deposition of Pt, followed by ion beam induced deposition of Pt. The sample was thinned at successively lower accelerating voltages, with final thinning performed at 5 kV. TEM experiments were performed on a ThermoFisher Spectra 300 probe aberration corrected S/TEM instrument equipped with a Super-X energy dispersive spectroscopy (EDS) silicon drift detector system with a 0.7 sr solid angle.

STEM DPC imaging was performed using a segmented STEM detector. In this imaging mode, electromagnetic fields and local variation of crystallographic orientation in the sample generate contrast due to spatial differences in beam deflection.[64, 66, 67, 79] The color wheel gives the vector orientation of the beam deflection, and the intensity of the color gives the magnitude. STEM DPC imaging has been used to image ferroelectric domains in AlScN,[7] and can provide information at the atomic scale.[64] PFM measurements were performed using a Bruker Dimension Icon atomic force microscope (AFM) using the PFM module. A lock-in frequency of 60 kHz and a drive amplitude ac bias of 10V was used for the PFM measurements. Height changes as a function of the AFM tip bias in pristine nanowires were used to measure the out-of-plane piezoresponse coefficient (d_{33})**;** dc bias poling was performed in the PFM mode by setting the ac bias to 100mV while applying a dc bias of +12V and – 12V separately in different regions to the AFM tip with respect to the grounded sample chuck. PFM measurements of the poled regions after applying the dc bias were performed to show residual changes to the piezoresponse due to ferroelectricity. Piezoresponse amplitude and phase hysteresis measurements were performed using a Bruker Signal Access Module (SAM) V and a lock-in amplifier (SRS 530). A 7 kHz frequency, 10V amplitude drive was applied as the tip bias and set as the lock-in reference signal, while the sample bias was swept using a 10V amplitude 1Hz triangle wave from a signal generator. The vertical signal output from the SAM was selected as input to the lock-in amplifier, which yielded amplitude and phase signals at the 7 kHz lock-in frequency.

Author Contributions

X. Zhang: writing – original draft, writing – review and editing, investigation, methodology, formal analysis; W. Xu: writing – original draft, writing – review and editing, investigation, methodology, formal analysis; A.C. Meng: conceptualization, writing – original draft, writing – review and editing, investigation, methodology, formal analysis; W.J. Meng: conceptualization, writing – original draft, writing – review and editing, investigation, methodology, formal analysis, funding acquisition. The manuscript was written through contributions of all authors.

Conflicts of interest

There are no conflicts to declare.

Acknowledgements

We acknowledge Dr. Yang Mu for assistance with XPS data acquisition. This work was funded in part by the NSF EPSCoR program, under awards OIA-1541079 and OIA-1946231, and by the Missouri Research Council, under award URC-23-012. Use of experimental facilities at the LSU Shared Instrumentation Facility (SIF), a part of the Louisiana Core User Facilities (CUF), is acknowledged. Use of experimental facilities at the MU Electron Microscopy Core (EMC) Facilities is acknowledged.

References

‡
§
§§

1. X. Liu, J. Zheng, D. Wang, P. Musavigharavi, E. A. Stach, R. Olsson, III and D. Jariwala, *Appl. Phys. Lett.*, 2021, **118**.
2. S. Fichtner, N. Wolff, F. Lofink, L. Kienle and B. Wagner, *J. Appl. Phys.*, 2019, **125**.
3. J. X. Zheng, M. M. A. Fiagbenu, G. Esteves, P. Musavigharavi, A. Gunda, D. Jariwala, E. A. Stach and R. H. Olsson, III, *Appl. Phys. Lett.*, 2023, **122**.
4. V. J. Gokhale, M. T. Hardy, D. S. Katzer and B. P. Downey, *IEEE Electron Device Lett.*, 2023, **44**, 674-677.
5. Y. Zou, C. Gao, J. Zhou, Y. Liu, Q. Xu, Y. Qu, W. Liu, J. B. W. Soon, Y. Cai and C. Sun, *Microsyst. Nanoeng.*, 2022, **8**, 124.
6. G. Esteves, T. R. Young, Z. Tang, S. Yen, T. M. Bauer, M. D. Henry and R. H. Olsson, III, *Appl. Phys. Lett.*, 2021, **118**.
7. X. Zhang, E. A. Stach, W. J. Meng and A. C. Meng, *Nanoscale Horiz.*, 2023, **8**, 674-684.
8. E. A. Mayer, O. Rogall, A. Ding, A. Nair, A. Žukauskaitė, P. D. Pupyrev, A. M. Lomonosov and A. P. Mayer, *Micromachines*, 2022, **13**, 1698.
9. A. Nair, M. Kessel, L. Kirste, N. M. Feil, M. Prescher and A. Žukauskaitė, *physica status solidi (a)*, 2022, **219**, 2200380.
10. N. Wolff, M. R. Islam, L. Kirste, S. Fichtner, F. Lofink, A. Žukauskaitė and L. Kienle, *Micromachines*, 2022, **13**, 1282.
11. M. T. Hardy, E. N. Jin, N. Nepal, D. S. Katzer, B. P. Downey, V. J. Gokhale, D. F. Storm and D. J. Meyer, *Applied Physics Express*, 2020, **13**, 065509.
12. P. Wang, D. Wang, N. M. Vu, T. Chiang, J. T. Heron and Z. Mi, *Appl. Phys. Lett.*, 2021, **118**.
13. E. N. Jin, A. C. Lang, B. P. Downey, V. J. Gokhale, M. T. Hardy, N. Nepal, D. S. Katzer and V. D. Wheeler, *J. Appl. Phys.*, 2023, **134**.
14. I. Streicher, S. Leone, C. Manz, L. Kirste, M. Prescher, P. Waltereit, M. Mikulla, R. Quay and O. Ambacher, *Crystal Growth & Design*, 2023, **23**, 782-791.
15. D. Wang, J. Zheng, Z. Tang, M. D. Agati, P. S. M. Gharavi, X. Liu, D. Jariwala, E. A. Stach, R. H. Olsson, V. Roebisch, M. Kratzer, B. Heinz, M. G. Han and K. Kisslinger, Ferroelectric C-Axis Textured Aluminum Scandium Nitride Thin Films of 100 nm Thickness, 2020 Joint Conference of the IEEE International Frequency Control Symposium and International Symposium on Applications of Ferroelectrics (IFCS-ISAF), 2020.
16. S. Satoh, K. Ohtaka, T. Shimatsu and S. Tanaka, *J. Appl. Phys.*, 2022, **132**.
17. C. S. Sandu, F. Parsapour, S. Mertin, V. Pashchenko, R. Matloub, T. LaGrange, B. Heinz and P. Muralt, *Phys. Status Solidi A*, 2019, **216**, 1800569.
18. M. Li, H. Lin, P. Luo, K. Hu, C. Liu, L. Chen and Y. Zhu, Texture evolution of ferroelectric AlScN films on metal under-layers, 2022 IEEE International Symposium on Applications of Ferroelectrics (ISAF), 2022.
19. E. Österlund, G. Ross, M. A. Caro, M. Paulasto-Kröckel, A. Hollmann, M. Klaus, M. Meixner, C. Genzel, P. Koppinen, T. Pensala, A. Žukauskaitė and M. Trebala, *Phys. Rev. Mater.*, 2021, **5**, 035001.
20. W. J. Meng, J. A. Sell, G. L. Eesley and T. A. Perry, *J. Appl. Phys.*, 1993, **74**, 2411-2414.
21. W. J. Meng, J. Heremans and Y. T. Cheng, *Appl. Phys. Lett.*, 1991, **59**, 2097-2099.
22. P. Musavigharavi, A. C. Meng, D. Wang, J. Zheng, A. C. Foucher, R. H. Olsson, III and E. A. Stach, *J. Phys. Chem. C*, 2021, **125**, 14394-14400.
23. K. Hiramatsu, K. Nishiyama, A. Motogaito, H. Miyake, Y. Iyechika and T. Maeda, *Phys. Status Solidi A*, 1999, **176**, 535-543.
24. D. Dede, F. Glas, V. Piazza, N. Morgan, M. Friedl, L. Güniat, E. Nur Dayi, A. Balgarkashi, V. G. Dubrovskii and A. Fontcuberta i Morral, *Nanotechnology*, 2022, **33**, 485604.
25. D. Kapolnek, S. Keller, R. Vetury, R. D. Underwood, P. Kozodoy, S. P. Den Baars and U. K. Mishra, *Appl. Phys. Lett.*, 1997, **71**, 1204-1206.
26. B. Beaumont, V. Bousquet, P. Vennéguès, M. Vaille, A. Bouillé, P. Gibart, S. Dassonneville, A. Amokrane and B. Sieber, *Phys. Status Solidi A*, 1999, **176**, 567-571.
27. S. Gradečak, P. Stadelmann, V. Wagner and M. Ilegems, *Appl. Phys. Lett.*, 2004, **85**, 4648-4650.
28. S. Tomiya, K. Funato, T. Asatsuma, T. Hino, S. Kijima, T. Asano and M. Ikeda, *Appl. Phys. Lett.*, 2000, **77**, 636-638.
29. I. Mahaboob, K. Hogan, S. W. Novak, F. Shahedipour-Sandvik, R. P. Tompkins and N. Lazarus, *J. Vac. Sci. Technol. B*, 2018, **36**.
30. P. D. Dapkus, C. Y. Chi, S. J. Choi, H. J. Chu, M. Dreiske, R. Li, Y. Lin, Y. Nakajima, D. Ren, R. Stevenson, M. Yao, T. W. Yeh and H. Zhao, *Prog. Quantum Electron.*, 2021, **75**, 100304.
31. R. D. Dupuis, *Science*, 1984, **226**, 623-629.
32. P. Aseev, A. Fursina, F. Boekhout, F. Krizek, J. E. Sestoft, F. Borsoi, S. Heedt, G. Wang, L. Binci, S. Martí-Sánchez, T. Swoboda, R. Koops, E. Uccelli, J. Arbiol, P. Krogstrup, L. P. Kouwenhoven and P. Caroff, *Nano Lett.*, 2019, **19**, 218-227.
33. S. Hertenberger, D. Rudolph, M. Bichler, J. J. Finley, G. Abstreiter and G. Koblmüller, *J. Appl. Phys.*, 2010, **108**.
34. E. A. Serban, J. Palisaitis, C.-C. Yeh, H.-C. Hsu, Y.-L. Tsai, H.-C. Kuo, M. Junaid, L. Hultman, P. O. Å. Persson, J. Birch and C.-L. Hsiao, *Sci. Rep.*, 2017, **7**, 12701.
35. E. A. Serban, J. Palisaitis, P. O. Å. Persson, L. Hultman, J. Birch and C.-L. Hsiao, *Thin Solid Films*, 2018, **660**, 950-955.
36. E. A. Serban, P. O. Åke Persson, I. Poenaru, M. Junaid, L. Hultman, J. Birch and C.-L. Hsiao, *Nanotechnology*, 2015, **26**, 215602.
37. K. L. Kavanagh, *Semicond. Sci. Technol.*, 2010, **25**, 024006.
38. A. C. Meng, C. S. Fenrich, M. R. Braun, J. P. McVittie, A. F. Marshall, J. S. Harris and P. C. McIntyre, *Nano Lett.*, 2016, **16**, 7521-7529.
39. A. C. Meng, M. R. Braun, Y. Wang, S. Peng, W. Tan, J. Z. Lentz, M. Xue, A. Pakzad, A. F. Marshall, J. S. Harris, W. Cai and P. C. McIntyre, *Mater. Today*, 2020, **40**, 101-113.
40. P. Caroff, M. E. Messing, B. Mattias Borg, K. A. Dick, K. Deppert and L.-E. Wernersson, *Nanotechnology*, 2009, **20**, 495606.
41. A. P. Vajpeyi, A. O. Ajagunna, G. Tsiakatouras, A. Adikimenakis, E. Iliopoulos, K. Tsagaraki, M. Androulidaki and A. Georgakilas, *Microelectron. Eng.*, 2009, **86**, 812-815.
42. S. Zhao, H. P. T. Nguyen, M. G. Kibria and Z. Mi, *Prog. Quantum Electron.*, 2015, **44**, 14-68.
43. K. Choi, M. Arita and Y. Arakawa, *J. Cryst. Growth*, 2012, **357**, 58-61.
44. H.-M. Wu and Y.-W. Peng, *Ceram. Int.*, 2015, **41**, 4847-4851.

45. G. A. Slack and T. F. McNelly, *J. Cryst. Growth*, 1976, **34**, 263-279.
46. W. Utsumi, H. Saitoh, H. Kaneko, T. Watanuki, K. Aoki and O. Shimomura, *Nat. Mater.*, 2003, **2**, 735-738.
47. M. Benjelloun, T. Sodhi, A. Kunti, L. Travers, A. Soltani, D. Morris, H. Maher, N. Gogneau and J. C. Harmand, Growth of Si-doped GaN Nanowires With Low Density For Power Device Applications, 2022 Compound Semiconductor Week (CSW), 2022.
48. E. Galopin, L. Largeau, G. Patriarche, L. Travers, F. Glas and J. C. Harmand, *Nanotechnology*, 2011, **22**, 245606.
49. C.-L. Hsiao, J. Palisaitis, M. Junaid, R.-S. Chen, P. O. Å. Persson, P. Sandström, P.-O. Holtz, L. Hultman and J. Birch, *Appl. Phys. Express*, 2011, **4**, 115002.
50. W. Zhu, J. Hayden, F. He, J.-I. Yang, P. Tipsawat, M. D. Hossain, J.-P. Maria and S. Trolier-McKinstry, *Appl. Phys. Lett.*, 2021, **119**.
51. S.-L. Tsai, T. Hoshii, H. Wakabayashi, K. Tsutsui, T.-K. Chung, E. Y. Chang and K. Kakushima, *Appl. Phys. Lett.*, 2021, **118**.
52. D. Drury, K. Yazawa, A. Zakutayev, B. Hanrahan and G. Brennecka, *Micromachines*, 2022, **13**, 887.
53. M. Yassine, A. Nair, J. Fammels, E. Wade, Z. Fu, A. Yassine, L. Kirste and O. Ambacher, *J. Appl. Phys.*, 2022, **132**.
54. W. J. Meng and G. L. Eesley, *Thin Solid Films*, 1995, **271**, 108-116.
55. R.-S. Chen, C.-C. Tang, C.-L. Hsiao, P. O. Holtz and J. Birch, *Appl. Surf. Sci.*, 2013, **285**, 625-628.
56. J. Chastain and R. C. King Jr, *Handbook of X-ray photoelectron spectroscopy*, 1992.
57. V. Serin, C. Colliex, R. Brydson, S. Matar and F. Boucher, *Phys. Rev. B*, 1998, **58**, 5106-5115.
58. L. A. Giannuzzi, *Introduction to focused ion beams: instrumentation, theory, techniques and practice*, Springer Science & Business Media, 2004.
59. C. Höglund, J. Bareño, J. Birch, B. Alling, Z. Czigány and L. Hultman, *J. Appl. Phys.*, 2009, **105**.
60. B. Alling, A. Karimi and I. A. Abrikosov, *Surf. Coat. Technol.*, 2008, **203**, 883-886.
61. K. Furuta, K. Hirata, S. A. Anggraini, M. Akiyama, M. Uehara and H. Yamada, *J. Appl. Phys.*, 2021, **130**.
62. K. Hirata, K. Shobu, H. Yamada, M. Uehara, S. A. Anggraini and M. Akiyama, *J. Eur. Ceram.*, 2020, **40**, 5410-5422.
63. K. A. Grossklaus, A. Banerjee, S. Jahangir, P. Bhattacharya and J. M. Millunchick, *J. Cryst. Growth*, 2013, **371**, 142-147.
64. J. A. Hachtel, J. C. Idrobo and M. Chi, *Adv. Struct. Chem. Imaging*, 2018, **4**, 10.
65. L. Chen, Z. Liang, S. Shao, Q. Huang, K. Tang and R. Huang, *Nanoscale*, 2023, **15**, 7014-7022.
66. N. Shibata, T. Seki, G. Sánchez-Santolino, S. D. Findlay, Y. Kohno, T. Matsumoto, R. Ishikawa and Y. Ikuhara, *Nat. Commun.*, 2017, **8**, 15631.
67. Q. Huang, Z. Chen, M. J. Cabral, F. Wang, S. Zhang, F. Li, Y. Li, S. P. Ringer, H. Luo, Y.-W. Mai and X. Liao, *Nat. Commun.*, 2021, **12**, 2095.
68. S. Barth, H. Bartzsch, D. Glöß, P. Frach, T. Modes, O. Zywitzki, G. Suchaneck and G. Gerlach, *Microsyst. Technol.*, 2016, **22**, 1613-1617.
69. O. Zywitzki, T. Modes, S. Barth, H. Bartzsch and P. Frach, *Surf. Coat. Technol.*, 2017, **309**, 417-422.
70. K. Umeda, H. Kawai, A. Honda, M. Akiyama, T. Kato and T. Fukura, Piezoelectric properties of ScAlN thin films for piezo-MEMS devices, 2013 IEEE 26th International Conference on Micro Electro Mechanical Systems (MEMS), 2013.
71. N. Balke, P. Maksymovych, S. Jesse, A. Herklotz, A. Tselev, C.-B. Eom, I. I. Kravchenko, P. Yu and S. V. Kalinin, *ACS Nano*, 2015, **9**, 6484-6492.
72. A. Gruverman, M. Alexe and D. Meier, *Nat. Commun.*, 2019, **10**, 1661.
73. S. Fichtner, F. Lofink, B. Wagner, G. Schönweger, T. N. Kreutzer, A. Petraru and H. Kohlstedt, Ferroelectricity in AlScN: Switching, Imprint and sub-150 nm Films, 2020 Joint Conference of the IEEE International Frequency Control Symposium and International Symposium on Applications of Ferroelectrics (IFCS-ISAF), 2020.
74. J. X. Zheng, D. Wang, P. Musavigharavi, M. M. A. Fiagbenu, D. Jariwala, E. A. Stach and R. H. Olsson, III, *J. Appl. Phys.*, 2021, **130**.
75. M. Pirro, G. Giribaldi, B. H. Soukup, X. Zhao, G. Michetti, W. Zhu, L. Colombo, C. Cassella and M. Rinaldi, Ferroelectric Considerations on Co-Sputtered 30% ALSCN with Different DC+RF Ratios, 2021 Joint Conference of the European Frequency and Time Forum and IEEE International Frequency Control Symposium (EFTF/IFCS), 2021.
76. J. Hayden, M. D. Hossain, Y. Xiong, K. Ferri, W. Zhu, M. V. Imperatore, N. Giebink, S. Trolier-McKinstry, I. Dabo and J.-P. Maria, *Phys. Rev. Mater.*, 2021, **5**, 044412.
77. W. Zhu, F. He, J. Hayden, J. I. Yang, P. Tipsawat, J.-P. Maria and S. Trolier-McKinstry, *Appl. Phys. Lett.*, 2023, **122**.
78. B.-R. Yeom, R. Navamathavan, J.-H. Park, Y.-H. Ra and C.-R. Lee, *CrystEngComm*, 2012, **14**, 5558-5563.
79. I. MacLaren, L. Wang, D. McGrouther, A. J. Craven, S. McVitie, R. Schierholz, A. Kovács, J. Barthel and R. E. Dunin-Borkowski, *Ultramicrosc.*, 2015, **154**, 57-63.